ADVANCED HEALTHCARE MATERIALS
www.advhealthmat.de

Hydrogel Microparticle-Templated Anti-Solvent Crystallization of Small-Molecule Drugs

Meghali Bora, Myat Noe Hsu, Saif A Khan, and Patrick S Doyle**

Conventional formulation strategies for hydrophobic small-molecule drug products frequently include mechanical milling to decrease active pharmaceutical ingredient (API) crystal size and subsequent granulation processes to produce an easily handled powder. A hydrogel-templated anti-solvent crystallization method is presented for the facile fabrication of microparticles containing dispersed nanocrystals of poorly soluble API. Direct crystallization within a porous hydrogel particle template yields core–shell structures in which the hydrogel core containing API nanocrystals is encased by a crystalline API shell. The process of controllable loading (up to 64% w/w) is demonstrated, and tailored dissolution profiles are achieved by simply altering the template particle size. API release is well described by a shrinking core model. Overall, the approach is a simple, scalable and potentially generalizable method that enables novel means of independently controlling both API crystallization and excipient characteristics, offering a "designer" drug particle system.

1. Introduction

With 40% of marketed drugs and 70–90% of newly identified compounds in the pharmaceutical drug pipeline being hydrophobic,[1] it is imperative for drug product formulation technologies to focus on improving drug bioavailability and efficacy. Although hydrophobic active pharmaceutical ingredients (APIs) can be converted into water-soluble salt forms, this approach remains largely incompatible with many APIs.[1b,2] In contrast, nanocrystal formation is a more general way to enhance solubility and dissolution rates owing to the large curvatures and surface areas in this size range (<1000 nm).[3] Nanocrystalline drugs also have the added advantage of solid-state stability as compared to their amorphous counterparts, and they are relatively stable to polymorphic transformation.[4]

Traditionally, to produce nanocrystalline drugs, bulk API crystallization is first performed in a controlled manner to ensure a therapeutically relevant polymorph with high purity. Nanocrystals are then produced through energy-intensive size reduction operations such as comminution, milling and high-pressure homogenization (with surfactants).[5] These nanocrystals are typically reformulated by blending with suitable excipient(s) before being compacted into preferred solid dosage forms. In addition to being cost-ineffective and time-consuming, associated drawbacks of these techniques include contamination due to erosion of milling beads, undesirable amorphous or polymorphic transformation, agglomeration and unintended alterations to release profiles.[6] Therefore, process intensification approaches that can directly produce commercially viable solid dosage forms are highly preferred. Recently, droplet-based crystallization has been extensively explored whereby emulsions containing dissolved drug and excipients undergo solvent removal, producing crystalline microparticles of desired form in a single step. This solvent removal is generally performed via thin-film evaporation in an immiscible continuous phase[7] or extractive crystallization using partially immiscible anti-solvents.[8] The resulting particles are spherical and highly uniform in nature, and hence they possess excellent processability; the binder excipient material contained in the microparticles further helps in maintaining the shape and structural integrity during the crystallization process.[8a] However, these droplet-based techniques remain limited in their choice of solvent pairs and operation temperatures to ensure emulsion stability throughout the crystallization process.

Among the various binder excipient materials, biocompatible polymeric hydrogels have been widely used in pharmaceutical formulations as drug carriers that modify release[9] or as

M. Bora, M. N. Hsu, S. A Khan, P. S Doyle
Singapore-MIT Alliance for Research and Technology
1 CREATE Way, #04-13/14 Enterprise Wing, Singapore 138602, Singapore
E-mail: saifkhan@nus.edu.sg; pdoyle@mit.edu
S. A Khan
Department of Chemical and Biomolecular Engineering
National University of Singapore
1 CREATE Way, #04-13/14 Enterprise Wing, Singapore 138602, Singapore
P. S Doyle
Department of Chemical Engineering
Massachusetts Institute of Technology
77 Massachusetts Avenue Room E17-504F, Cambridge, MA 02139, USA
P. S Doyle
Harvard Medical School Initiative for RNA Medicine
Boston, MA 02115, USA

The ORCID identification number(s) for the author(s) of this article can be found under https://doi.org/10.1002/adhm.202102252

DOI: 10.1002/adhm.202102252

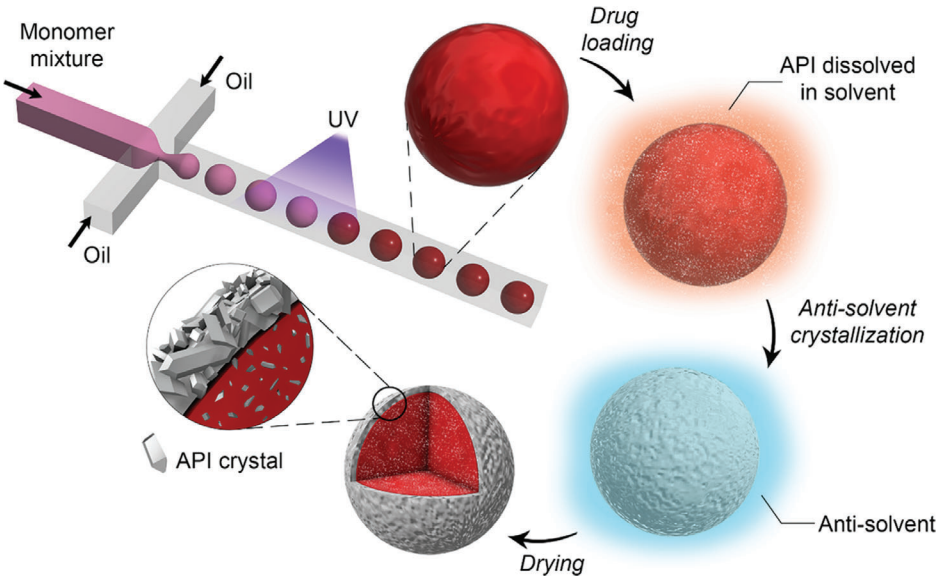

Figure 1. Schematic outlining the production methodology of core–shell drug particles.

heteronucleants for controlled crystallization.[10] Hydrogel matrices are gaining traction in drug product development, since their structure, topology, mesh size and chemical composition can be easily modified by existing synthesis methods. This enables tuning of the nucleation kinetics, nanocrystal size and loading by introducing confinement effects with the matrix pores and by thermodynamic partitioning driven by favorable polymer-solute interactions.[11] In particular, poly(ethylene glycol) diacrylate (PEGDA) hydrogels have been successful in controlling crystal size and polymorph for some APIs.[11b,12] Furthermore, with various modifications such as hydrophobic or micellar domains and drug-laden nanoemulsion encapsulation, high drug loading has also been achieved for hydrophobic APIs.[10a,b,12b,13] Hydrogel-based crystallization studies for hydrophobic APIs thus far have focused on controlling crystal size and polymorphic form by using evaporative and cooling crystallization methods; these methods are not feasible for heat or cold-labile drugs. An alternative is to employ anti-solvent techniques that can achieve crystallization at ambient conditions with rapid generation of high supersaturation regions. Unfortunately, bulk approaches involve simultaneous droplet generation and particle formation in stirred batches, often resulting in non-uniform particles. Here, we demonstrate the utility of porous hydrogel particles as templates upon which direct anti-solvent crystallization can be performed to obtain uniform and monodispersed drug microparticles.

In this study, uniformly-sized photo-crosslinked PEGDA hydrogel microparticles, fabricated via droplet microfluidics, served as the 3D template for drug loading and crystallization. Hydrogel particles were first swollen in an organic solvent containing a model hydrophobic API, fenofibrate (FEN). Upon addition of an anti-solvent, drug nanocrystals were formed within the pores of the matrix. A notable feature of this method was the formation of core–shell crystalline particles. While the core of hydrogel network contained nanocrystals as intended, drug-solvent removal to the surrounding anti-solvent coupled with the poor solubility of the drug gave rise to drug crystallization at the surface of the hydrogel particles. We report detailed characterization of the morphology, size, API loading, crystallinity and release profiles of these core–shell microparticles. In general, it was observed that the template particle size could tailor API loading as well as the volume fraction of the crystalline shell; this in turn allows for the control of drug release kinetics. Overall, our strategy is a facile and highly effective method for producing uniform and controllable spherical drug products. These particles have the capacity for versatile drug loading and we envision this scalable process to pave the way for designer pharmaceutical drug product manufacturing.

2. Results and Discussion

2.1. Nanocrystal-Laden Microparticle Synthesis

Using porous hydrogel microparticles as templates for small molecule API crystallization is a versatile approach for a variety of protocols involving various solvents and temperatures. The 3D network of microgel matrices allows for high drug loading while the relative ease of modification and functionalization can enable tailored API/excipient formulations. Most importantly, the synthesis, loading and dissolution of these composite microparticles are independent processes, enabling independent fine-tuning of their desired properties. **Figure 1** illustrates the sequential steps employed in fabricating the nanocrystal-containing microparticles. Briefly, pre-fabricated template microparticles (via droplet microfluidics) were first swollen with a drug solution. The excess solvent was then replaced with an anti-solvent to induce supersaturation, and hence crystallization of API occurred within the 3D gel template. A notable feature of this method was the formation of core–shell crystalline particles which will be discussed in detail in the following sections.

The template PEGDA microgels were produced using scalable emulsion polymerization using UV light in a cross-junction droplet generator. By tuning the flow ratio of the dispersed and continuous phase (DP and CP) or the physical dimensions of the

Table 1. Summary of the experimental conditions used in template particle production.

Particle size [μm]	Device	CP	Q_{CP} [μL min^{-1}]	Q_{DP} [μL min^{-1}]
200	200 μm PDMS cross-junction with 300 μm outlet tubing (Figure S1, Supporting Information)	HFE7500 with Pico-surf 1	12	6
600	1/32″ PEEK cross-junction with 1 mm outlet tubing	Silicone oil	400	20
1200	1/8″ PEEK cross-junction with 3 mm outlet tubing	Silicone oil	600	30

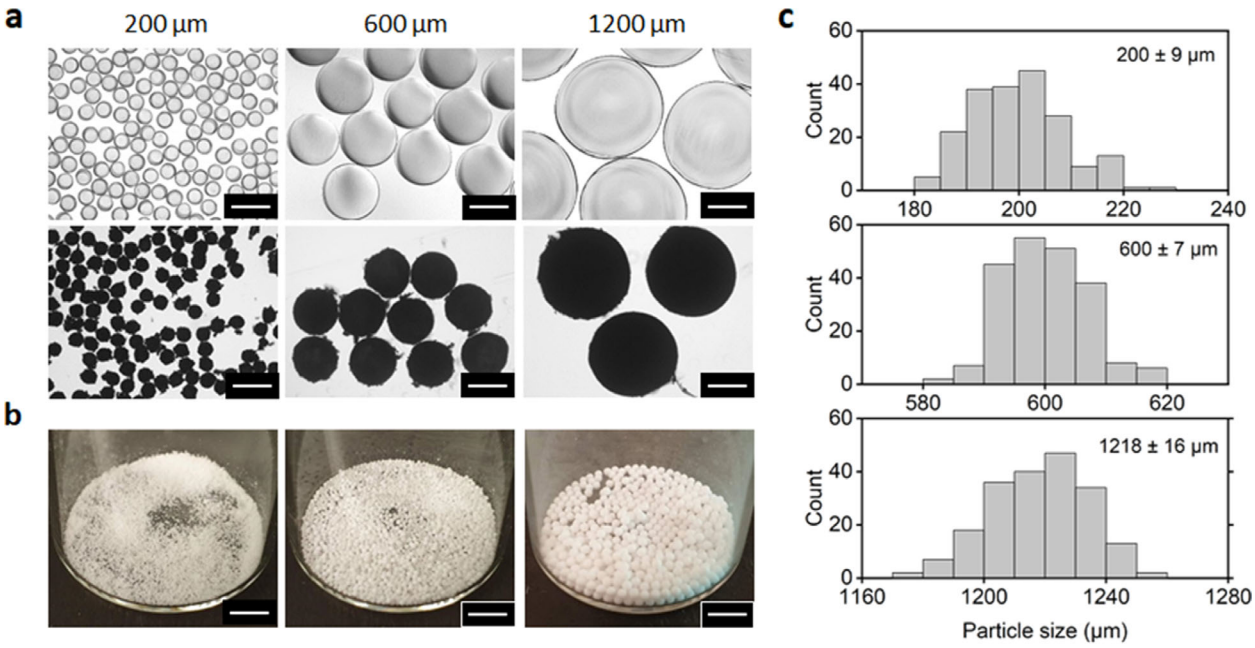

Figure 2. a) Optical microscopy images of swollen hydrogel intermediates before crystallization (top) and FEN loaded microparticles (bottom). Each scale bar represents 500 μm. b) Images of dried monodisperse and spherical FEN loaded PEGDA microparticles. Each scale bar represents 5 mm. c) Particle size distribution of dried FEN loaded PEGDA microparticles ($n = 200$).

droplet generator, various PEGDA particle sizes could easily be obtained. Here, we used three different sizes of cross-junctions to produce three nominal sizes of emulsion droplets that we classified as "200," "600," and "1200 μm." The exact experimental conditions used are summarized in **Table 1**. PEGDA particles began as a pre-polymer solution consisting of monomer PEGDA (Mn = 700 g mol^{-1}), porogen–poly (ethylene glycol) (PEG) (Mn = 200 g mol^{-1}), photoinitiator and stabilizer F127. This solution was sheared and emulsified in an immiscible CP at the microfluidic cross-junction. The resulting pre-polymer droplets were UV-polymerized while flowing through the outlet tubing. The microgels were then washed sufficiently in ethanol to remove CP and other unreacted chemicals.

The washed PEGDA particles were then loaded with a hydrophobic API by swelling them overnight with a suitable organic solvent containing dissolved API. This protocol was to ensure equilibrium partitioning of the drug into the hydrogel. FEN was used as the model API in this work due to its extensive use in previous studies. Recent studies that correlate the FEN crystal size with its melting point[14] were used to estimate the nanocrystal sizes in the core–shell particles. Ethyl acetate (EA) was chosen as the organic solvent due to its high saturation concentration of FEN and its ability to penetrate into PEGDA networks.[12b,15] Next, excess FEN solution was removed, and anti-solvent——distilled water——was immediately added to facilitate solvent removal from the template hydrogel mesh at ambient temperature, resulting in FEN supersaturation and hence crystallization within the hydrogel pores (see Videos S1 and S2, Supporting Information). Optical images showed that the transparent template PEGDA particles turned opaque upon crystallization and drying (**Figure 2**a). The cross-linked template microgels remained mechanically stable and maintained their spherical shape throughout the entire process (Figure 2b), resulting in API-laden microparticles with excellent flow properties (see Video S3, Supporting Information). Additionally, the dried microparticles are highly uniform with tightly controlled sizes and distributions: $d = 200 \pm 9$ μm, 600 ± 7 μm, and 1218 ± 16 μm (Figure 2c) under the specific conditions noted in Table 1. This approach thus highlighted the efficacy of droplet microfluidics in generating uniform and stable microgel templates for direct API crystallization.

2.2. Characterization of API Crystals within Microgels

The 3D network of the hydrogel matrix contained significant void spaces and domains within which API crystallization could take

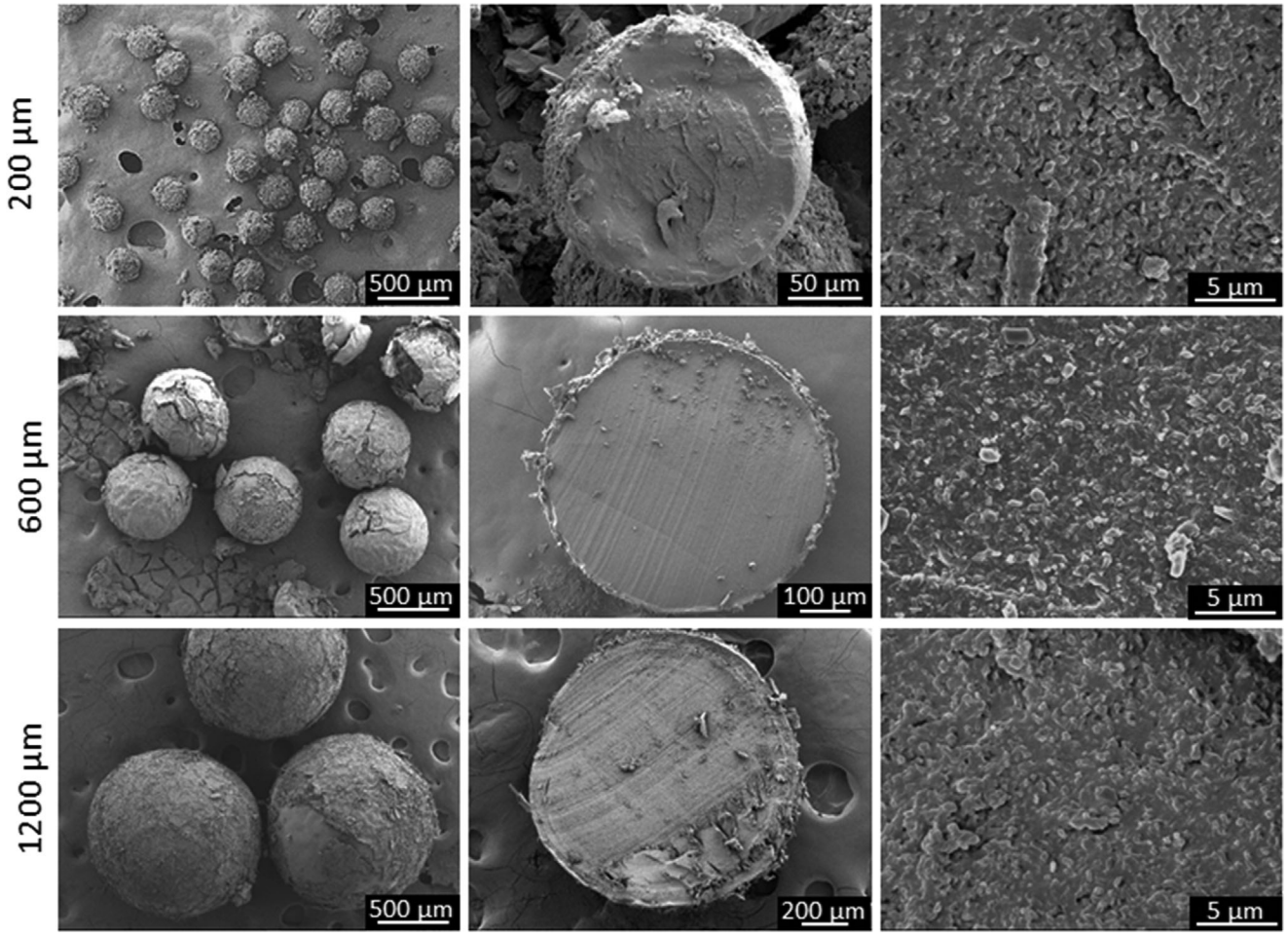

Figure 3. FESEM images of FEN-loaded PEGDA particles. The leftmost column shows the overview morphology of the dried particles. The middle column shows interior surfaces of carefully cut particles. The crystalline shell could be observed surrounding each particle. The rightmost column shows cross-sectional views where nanocrystals were observed to be embedded within the particle matrix.

place. The presence of FEN crystals in the microgel matrices was confirmed by field emission scanning election microscopy (FESEM) imaging. In addition to nanocrystals embedded within the hydrogel mesh, a crystalline shell consisting of larger FEN crystals was also observed around each microparticle (**Figure 3**). We hypothesize that solvent diffusion from the hydrogel matrix into the surrounding water (anti-solvent) causes some of the entrapped API to diffuse out of the particles before crystallization can take place. Coupled with the API's poor solubility in water, this gives rise to a high local FEN concentration, leading to significant crystal formation at the surface of the hydrogel particles. Hence, a crystalline drug shell was formed that encases the excipient microparticle with nanocrystals in its pores. The presence of the shell was further confirmed by polarized microscopy images which showed bright crystalline rims surrounding the particles (see Figure S2, Supporting Information). The unique core–shell structure was observed regardless of the speed of anti-solvent addition to the API swollen particles. In fact, we observed a similar particle morphology under both static and stirred conditions (see Videos S3 and S4, Supporting Information), highlighting the consistency of this technique. Crystalline shell volume fraction was estimated by subtracting particle size before and after the removal of the shell through probe-sonication. Interestingly, the shell volume fraction varied significantly across microparticle sizes: 0.53, 0.15, and 0.08 for 200, 600, and 1200 µm particles, respectively (see Figure S3, Supporting Information). This allows the tailoring of API dissolution profile by simply adjusting the particle size. In typical situations, a crystalline shell gives rise to a burst release while embedded nanocrystals would diffuse slowly from the hydrogel matrix. Accordingly, particle size, which could be controlled using various droplet forming conditions, could be utilized to further fine-tune API release profiles with relative ease by targeting a particular ratio of shell-to-embedded crystals.

To confirm the crystallinity of FEN, PEGDA particles were characterized by powder X-ray diffraction (XRD). **Figure 4** shows the background-subtracted powder XRD spectra of bulk FEN (form I) and FEN-loaded PEGDA particles. Across all PEGDA particle sizes, FEN form 1 was obtained as seen from the characteristic peaks in the XRD spectra at 12°, 14.5°, 16.2°, 16.8°, and 22.4° (marked with green asterisks in Figure 4).[15,16] Raw XRD spectra before background subtraction are provided in Figure S4, Supporting Information. Although only FEN form 1 was

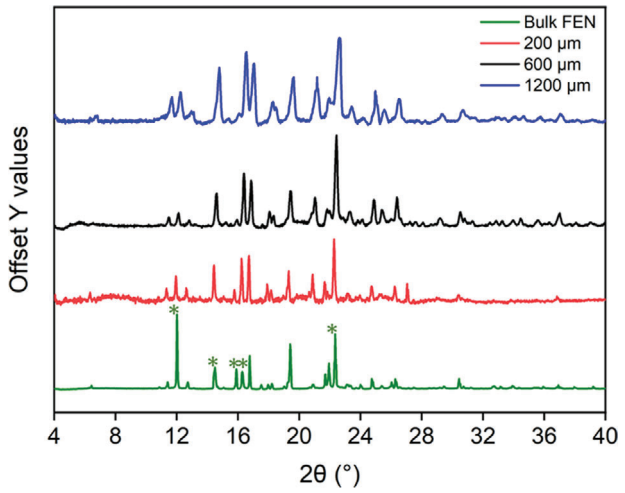

Figure 4. Background-subtracted powder XRD spectra of bulk FEN and FEN loaded PEGDA particles. The characteristic peaks of FEN form I are marked with asterisks.

present, differential scanning calorimetry (DSC) curves revealed two melting peaks, especially for 600 and 1200 μm particles (**Figure 5**a). The two distinct peaks can be attributed to the presence of two populations of crystal sizes according to the melting point depression phenomena commonly observed in nanomaterials (Figure 5a inset). Particularly, the lower and higher temperature peak represent the nanocrystals in the matrix and larger crystals in the particle shell respectively. As the shell volume fraction of the particles increased with reduction in particle size, the higher temperature peak became more dominant. For the smallest size (200 μm) particles, the lower temperature peak was no longer observable. Prior works have studied the relationship between FEN crystal size and its melting point, and data from these studies were used as a calibration curve to estimate the crystal sizes from the observed DSC melting peaks.[12b,14] Using the DSC melting peaks, the nanocrystal population in the PEGDA matrix was estimated to be ≈50 nm in size while the shell contained crystals of ≈120 nm size. Prior work by our group has shown that these polymer systems undergo microphase separation during polymerization giving rise to two length-scales within the gel matrix.[11a] The 50 nm nanocrystal size we find in the matrix is approximately equivalent to the larger gel matrix length scale. However, it is important to note that the DSC peaks obtained were rather broad, especially at the higher temperature and thus were likely the cumulative effect of a distribution of crystal sizes. In addition, the ability to predict the size of nanocrystals from DSC data diminishes for larger crystal sizes.[14] FESEM images in Figure 3 confirm the presence of uniformly-distributed nanocrystals throughout the matrix. Individual crystals in the shell are difficult to discern due to the consolidated structure.

In addition to shell volume fraction, particle size variation had an influence on FEN loading as measured by thermogravimetric analysis (TGA). The TGA curve for bulk FEN showed a single step mass loss at around 292 °C[17] while there was minimum PEGDA mass loss at this temperature (see Figure S5, Supporting Information). Thus, each step of the TGA curves for FEN-loaded PEDGA particles was evaluated to determine the mass loading of FEN (Figure 5b). Counterintuitively, smaller microparticles had greater mass loading (Figure 5c). We hypothesized that FEN flux out of the PEGDA particles during the anti-solvent crystallization step was the greatest for 200 μm particles, leading to rapid precipitation and formation of the crystalline shell and hence less FEN was lost to the surrounding water. Accordingly, FEN mass loading for the 200 μm particles (64% w/w) was the closest to the theoretical maximum drug loading (75% w/w) (see Section S2, Supporting Information). On the other hand, larger particles with smaller outward FEN flux led to more drug loss during the crystallization step; 600 μm particles had 41% w/w while 1200 μm particles had 25% w/w FEN loading. Hence, depending on the required API release profiles for effective delivery, a pre-determined particle size could be engineered to achieve a desired drug load.

2.3. Characterization of Dissolution Kinetics

Dissolution studies were carried out in simulated gastric fluids (SGF) at 37 °C following a previously established protocol.[10b,12] In order to ensure sink conditions, the amount of particles suspended were calculated to ensure that the maximum FEN concentration at the end of the release study would remain at 30 μg mL^{-1}, which is well below the saturation concentration (193 μg mL^{-1}). Moreover, the acidic nature SGF (pH 1.2) prevented the hydrolysis of PEGDA, thus maintaining the particle structural integrity. As such, the release solely depended on the FEN dissolution and diffusion into the SGF.

The obtained in vitro dissolution profiles indicated large initial release rates as the crystalline shell was not protected by any matrix material to hinder diffusion (**Figure 6**a). Overall, 200 μm particles had significantly faster release rates as the volume fraction of crystal shell was the greatest. The larger surface area afforded by the smaller particle size also facilitated the release of FEN from the matrix. Optical images taken at various points revealed that the FEN release closely follows the shrinking-core constant particle-size model[18] (Figure 6a; Figure S6, Supporting Information) once the dissolution of the outer shell is completed. It was observed that SGF dissolved the FEN crystals progressively from the particle surface. As the dissolution progressed, a hydrogel region freed of FEN crystals formed on the outer periphery of the particles, gradually resulting in a shrinking FEN core. The model assumes that dissolution generally occurs in four steps: 1) dissolution of FEN from the crystal core in the hydrogel matrix, 2) diffusion of FEN molecules from the crystal core/hydrogel interface through the hydrogel, 3) diffusion of FEN molecules from the hydrogel/SGF interface through a thin surface boundary layer, and 4) diffusion of FEN molecules from the surface boundary layer/bulk SGF interface to bulk SGF. Here, we assumed that the diffusion resistance due to the thin surface boundary layer compared to the hydrogel matrix was negligible. We then fitted the dissolution data to the model using previously reported calculations [19]

$$\frac{t}{\tau} = \left(1 - 3r_c^{*2} + 2r_c^{*3}\right) \quad (1)$$

$$1 - X = \frac{V_{core}}{V_{particle}} = r_c^{*3} \quad (2)$$

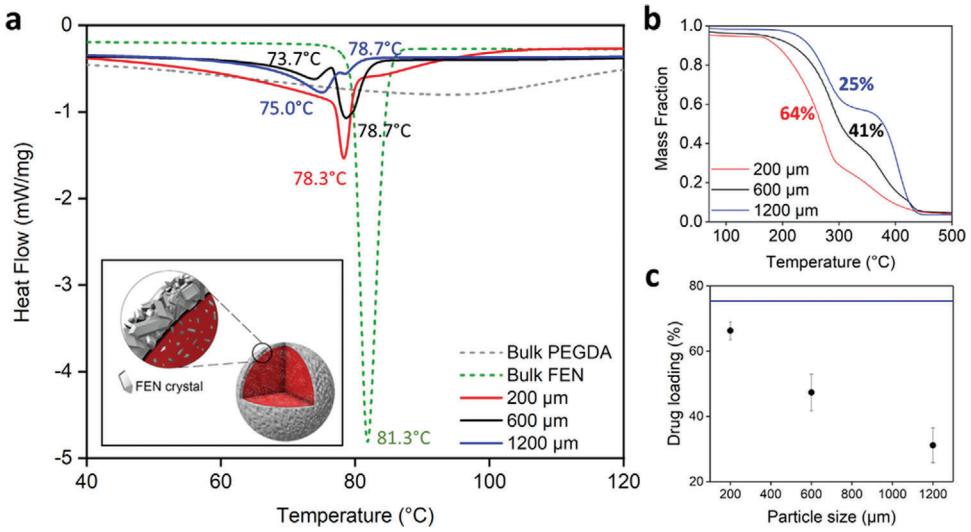

Figure 5. a) DSC curves showing two distinct melting peaks corresponding to the two different crystal size populations. Inset schematic illustrates the two crystal populations in the matrix and surrounding shell (not to scale). b) Representative TGA curves for FEN-loaded PEGDA particles. 200, 60, and 1200 µm particles have 64%, 41%, and 25% (w/w) FEN loading respectively. c) FEN mass loading in hydrogels. Blue line represents the estimated theoretical maximum drug loading. Error bars represent standard deviation of each group ($n = 3$).

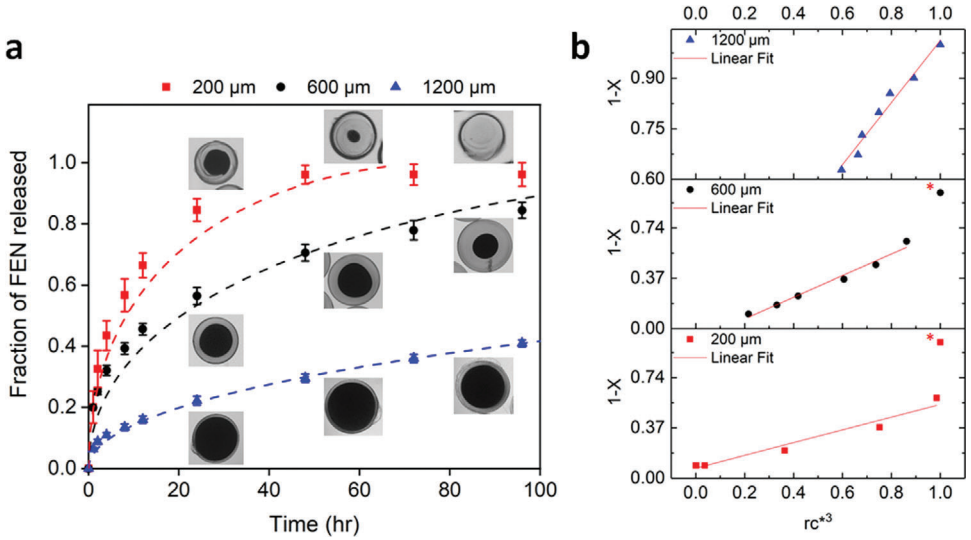

Figure 6. a) Dissolution profiles of FEN loaded PEGDA particles in SGF. The data were fitted to the shrinking-core model (dashed lines). Error bars represent standard deviations for each group ($n = 3$). b) Observed shrinkage of FEN crystal core fitted to the shrinking-core model (up to 96 h release). * indicates the data not included in the linear fit.

where t is dissolution time, τ is the time for complete dissolution, r_c* is the dimensionless radius given by $r_{core}/r_{particle}$ and X is the fraction of FEN released at time t. The model estimated that the complete dissolution times for 200, 600, and 1200 µm particles were 3.2 days, 7.7 days and 76 days, respectively. Experimentally, complete dissolution was achieved in 4 days for 200 µm particles, 8 days for 600 µm particles and 46 days for 1200 µm particles. The disparity for the 1200 µm particles can be attributed to an observed swelling of the free hydrogel region, which likely reduces the diffusion resistance and facilitates faster release. Figure 6b compares the experimentally measured fraction of FEN released with the measured shrinking core radii. The shrinking core model fits all cases quite closely, with deviations only observed at the earliest times due to the presence of a prominent shell, especially for the 200 and 600 µm particles (as marked out with an asterisk in Figure 6b). Generally, these results highlight the influence of the crystal shell volume fractions, which can be easily tuned, on the dissolution profiles.

3. Concluding Remarks

We successfully demonstrated a method for direct anti-solvent crystallization in microgel scaffolds for formulation of microparticles containing water-insoluble API nanocrystals. The resulting

core–shell structure of the microparticles could be tuned via the overall particle size, with reduction in particle size being associated with a greater shell volume fraction. This resulted in various degrees of drug loading, with the smallest particles corresponding to the highest drug load (≈64% w/w). In addition, varying shell volume fractions enabled further fine-tuning of drug release profiles with relative ease; crystalline shells typically lead to burst release behavior while the embedded nanocrystals diffuse slowly from the hydrogel matrix. As a result, the dissolution rate decreased with increasing particle size due to the dominant nanocrystal population in the matrix. Importantly, the template particle production using droplet microfluidics is a scalable process with many available high-throughput emulsion generator designs,[20] allowing the fabrication at industrially relevant scales. In conclusion, our hydrogel-templated anti-solvent crystallization strategy can produce highly uniform and controllable spherical drug products/intermediates with high yield in a relatively simple, cost-effective, and scalable manner. Furthermore, by decoupling the excipient particle formation and drug crystallization, this technique enables independent fine-tuning of their desired properties.

4. Experimental Section

Materials: Poly (ethylene glycol) diacrylate (PEGDA, Mn = 700 g mol^{-1}), poly (ethylene glycol) (PEG, Mn = 200 g mol^{-1}), 2-hydroxy-2-methylpropiophenone (HMP), Pluronic F-127 (F127), fenofibrate (FEN), ethyl acetate (EA), sodium phosphate monobasic, and sodium dodecyl sulfate (SDS) were purchased from Sigma-Aldrich, Singapore. Silicone Fluid PMX-200 (10 cSt) was purchased from XIAMETER, Singapore. Fluorinated surfactant Pico-surf 1 was purchased from Sphere Fluidics Limited and fluorinated oil HFE7500 was purchased from 3M, Singapore. Ethanol, acetone and hydrochloric acid (HCl) were purchased from VWR Singapore. All chemicals were used as received.

Fabrication of Drug Loaded PEGDA Hydrogel Microparticles: The fabrication method for hydrogel microparticles is similar to an earlier report from our group with a few modifications.[12b] In brief, the precursor solution (dispersed phase, DP) for hydrogels was prepared by dissolving 20% (v/v) PEGDA, 20% (v/v) PEG, 1% (v/v) photoinitiator HMP in 2% (w/v) F127 solution in ultrapure water. The continuous phase (CP) was one of the following: 1) silicone oil or 2) 0.15% (v/v) pico-surf 1 in HFE7500. The DP and CP were filtered through 0.2 µm nylon and 0.45 µm polytetrafluoroethylene (PTFE) syringe filters respectively before each experiment. Droplets were then generated by flowing the DP and CP through a MicroCross PEEK microfluidic cross-junction or PDMS cross-junction device. The specific conditions used to generate different droplet sizes are summarized in Table 1. The generated droplets were crosslinked into hydrogel microparticles while flowing through the outlet tubing exposed to a UV lamp (VL-215-LM, 15 W, 365 nm; Vilber Lourmat) for ≈34 s. The resulting hydrogel particles were separated from the CP by washing in absolute ethanol three times over a period of 24 h. Afterward, the particles were soaked in EA three times for 24 h. For drug loading, the particles were transferred into a FEN in EA solution (400 mg mL^{-1}) for 24 h at room temperature to ensure homogenous loading. The next day, after excess FEN solution was removed, water—the anti-solvent—was added immediately to induce crystallization. The solvent–antisolvent exchange was allowed to continue for 15 min at room temperature. The resulting crystalline particles were then dried under vacuum at room temperature for 24 h.

Experimental Characterization: The polymorphism of crystalline FEN within the hydrogel microparticles was characterized by powder X-ray diffraction (XRD) raging from a 2θ angle of 4°–40° at a scan rate of 1° min^{-1}. Particle size distribution was determined by FIJI[21] using optical upright microscopy images. Particle and crystal morphology were characterized using a field emission scanning election microscopy (FESEM, 7610, JEOL). Prior to FESEM observation at operating voltage 5 kV, dried samples were carefully cut to expose their internal morphology and sputter coated with a platinum layer. Next, crystal size populations were identified through a DSC thermogram using DSC25 with Tzero pans from TA instruments. Each sample was equilibrated at −20 °C for 5 min before heating from −20 to 125 °C at a rate of 10 °C min^{-1}. Previously published data correlating melting points to nanocrystal sizes[14] were used as a calibration curve to determine crystal size distribution. Lastly, FEN loadings in final dried samples were determined from TGA curves (Mettler Toledo) from 40 to 500 °C at a heating rate of 10 °C min^{-1}.

Drug Dissolution Experiment: FEN mass loading (w/w) of microparticles was first determined before each dissolution experiment. Afterward, the particles were suspended in 40 mL of simulated gastric fluid (SGF) (50×10^{-3} M sodium phosphate monobasic, 25×10^{-3} M SDS, pH 1.2). SDS was added to ensure sink conditions by significantly increasing the saturation concentration of FEN in aqueous media, following previously established protocols.[10b,12b,13] The mass of particles suspended in SGF was calculated to ensure that the final FEN concentration after drug release would remain at 30 µg mL^{-1}, which is well below the saturation concentration (193 µg mL^{-1}). The particles were stirred using an orbital shaker at 200 rpm at 37 °C throughout the dissolution study. At specified timepoints, 600 µL samples were temporarily taken out to measure the amount of FEN released using a Cary 60 UV–vis spectrophotometer. The concentration of FEN released was quantified using the UV absorbance at 290 nm. A calibration curve of FEN in SGF in the concentration range of 1 to 100 µg mL^{-1} was also prepared (Figure S7, Supporting Information).

Statistical Analysis: All the data were represented as the mean ± standard deviation. The sample size (n) for each analysis has been described in the corresponding figure captions.

Supporting Information

Supporting Information is available from the Wiley Online Library or from the author.

Acknowledgements

M.B. and M.N.H. contributed equally to this work. This research was supported by the National Research Foundation, Prime Minister's Office, Singapore under its Campus for Research Excellence and Technological Enterprise program. Financial support was also provided by the Pharmaceutical Innovation Programme Singapore (grant number A19B3a0012).

Conflict of Interest

The authors declare no conflict of interest.

Data Availability Statement

The data that support the findings of this study are available from the corresponding author upon reasonable request.

Keywords

crystallization, hydrogels, microparticles, nanocrystals, small molecule drugs

Received: October 19, 2021
Revised: December 14, 2021
Published online:

[1] a) A. M. Thayer, *Chem. Eng. News Arch.* **2010**, *88*, 13; b) S. Kalepu, V. Nekkanti, *Acta Pharm. Sin. B* **2015**, *5*, 442.
[2] S. Stegemann, F. Leveiller, D. Franchi, H. De Jong, H. Lindén, *Eur. J. Pharm. Sci.* **2007**, *31*, 249.
[3] L. Gao, D. Zhang, M. Chen, *J. Nanopart. Res.* **2008**, *10*, 845.
[4] T. Van Duong, G. Van den Mooter, *Expert Opin. Drug Delivery* **2016**, *13*, 1583.
[5] a) J. Chen, B. Sarma, J. M. Evans, A. S. Myerson, *Cryst. Growth Des.* **2011**, *11*, 887; b) L. Peltonen, J. Hirvonen, *J. Pharm. Pharmacol.* **2010**, *62*, 1569; c) H. De Waard, W. Hinrichs, H. Frijlink, *J. Controlled Release* **2008**, *128*, 179.
[6] a) A. Y. Lee, D. Erdemir, A. S. Myerson, *Annu. Rev. Chem. Biomol. Eng.* **2011**, *2*, 259; b) M. Warman, Continuous Processing in Secondary Production. *Chem. Eng. Pharm. Ind.*, Chemical Engineering in the Pharmaceutical Industry: R&D to Manufacturing, **2010**, 837–851. c) H. Valo, S. Arola, P. Laaksonen, M. Torkkeli, L. Peltonen, M. B. Linder, R. Serimaa, S. Kuga, J. Hirvonen, T. Laaksonen, *Eur. J. Pharm. Sci.* **2013**, *50*, 69.
[7] a) R. A. Leon, A. Z. M. Badruddoza, L. Zheng, E. W. Yeap, A. I. Toldy, K. Y. Wong, T. A. Hatton, S. A. Khan, *Cryst. Growth Des.* **2015**, *15*, 212; b) E. W. Yeap, D. Z. Ng, A. Prhashanna, A. Somasundar, A. J. Acevedo, Q. Xu, F. Salahioglu, M. V. Garland, S. A. Khan, *Cryst. Growth Des.* **2017**, *17*, 3030; c) A. I. Toldy, L. Zheng, A. Z. M. Badruddoza, T. A. Hatton, S. A. Khan, *Cryst. Growth Des.* **2014**, *14*, 3485.
[8] a) T. Gu, E. W. Yeap, Z. Cao, D. Z. Ng, Y. Ren, R. Chen, S. A. Khan, T. A. Hatton, *Adv. Healthcare Mater.* **2018**, *7*, 1700797; b) E. W. Yeap, D. Z. Ng, D. Lai, D. J. Ertl, S. Sharpe, S. A. Khan, *Org. Process Res. Dev.* **2018**, *23*, 93.
[9] a) N. Peppas, P. Bures, W. Leobandung, H. Ichikawa, *Eur. J. Pharm. Biopharm.* **2000**, *50*, 27; b) M. N. Hsu, R. Luo, K. Z. Kwek, Y. C. Por, Y. Zhang, C.-H. Chen, *Biomicrofluidics* **2015**, *9*, 052601.
[10] a) H. B. Eral, V. López-Mejías, M. O'Mahony, B. L. Trout, A. S. Myerson, P. S. Doyle, *Cryst. Growth Des.* **2014**, *14*, 2073; b) H. B. Eral, M. O'Mahony, R. Shaw, B. L. Trout, A. S. Myerson, P. S. Doyle, *Chem. Mater.* **2014**, *26*, 6213; c) J. Ling, K. Chadwick, *Org. Process Res. Dev.* **2017**, *21*, 827.
[11] a) Y. Diao, M. E. Helgeson, Z. A. Siam, P. S. Doyle, A. S. Myerson, T. A. Hatton, B. L. Trout, *Cryst. Growth Des.* **2012**, *12*, 508; b) Y. Diao, M. E. Helgeson, A. S. Myerson, T. A. Hatton, P. S. Doyle, B. L. Trout, *J. Am. Chem. Soc.* **2011**, *133*, 3756.
[12] a) Y. Diao, K. E. Whaley, M. E. Helgeson, M. A. Woldeyes, P. S. Doyle, A. S. Myerson, T. A. Hatton, B. L. Trout, *J. Am. Chem. Soc.* **2012**, *134*, 673; b) P. D. Godfrin, H. Lee, J. H. Lee, P. S. Doyle, *Small* **2019**, *15*, 1803372.
[13] A. Z. M. Badruddoza, P. D. Godfrin, A. S. Myerson, B. L. Trout, P. S. Doyle, *Adv. Healthcare Mater.* **2016**, *5*, 1960.
[14] L. Dwyer, V. Michaelis, M. O'Mahony, R. Griffin, A. Myerson, *CrystEngComm* **2015**, *17*, 7922.
[15] S. Watterson, S. Hudson, M. Svärd, Å. C. Rasmuson, *Fluid Phase Equilib.* **2014**, *367*, 143.
[16] A. Heinz, K. C. Gordon, C. M. McGoverin, T. Rades, C. J. Strachan, *Eur. J. Pharm. Biopharm.* **2009**, *71*, 100.
[17] X. Feng, X. Ye, J.-B. Park, W. Lu, J. Morott, B. Beissner, Z. J. Lian, E. Pinto, V. Bi, S. Porter, *Drug Dev. Ind. Pharm.* **2015**, *41*, 1479.
[18] S. Schrank, A. Hodzic, A. Zimmer, B. J. Glasser, J. Khinast, E. Roblegg, *Aaps PharmSciTech* **2012**, *13*, 686.
[19] a) W.-L. Hsu, M.-J. Lin, J.-P. Hsu, *Int. J. Chem. Biol. Eng.* **2009**, *2*, 205; b) V. Safari, G. Arzpeyma, F. Rashchi, N. Mostoufi, *Int. J. Miner. Process.* **2009**, *93*, 79.
[20] a) E. Amstad, M. Chemama, M. Eggersdorfer, L. R. Arriaga, M. P. Brenner, D. A. Weitz, *Lab Chip* **2016**, *16*, 4163; b) E. Stolovicki, R. Ziblat, D. A. Weitz, *Lab Chip* **2018**, *18*, 132.
[21] J. Schindelin, I. Arganda-Carreras, E. Frise, V. Kaynig, M. Longair, T. Pietzsch, S. Preibisch, C. Rueden, S. Saalfeld, B. Schmid, *Nat. Methods* **2012**, *9*, 676.